The Astrophysical Journal, 867:117 (13pp), 2018 November 10 https://doi.org/10.3847/1538-4357/aae48b

The Dust-selected Molecular Clouds in the Northeast Region of the Small Magellanic Cloud*

Tatsuya Takekoshi[1,2], Tetsuhiro Minamidani[3,4], Shinya Komugi[5], Kotaro Kohno[1], Tomoka Tosaki[6], Kazuo Sorai[7], Erik Muller[8], Norikazu Mizuno[4,8,9], Akiko Kawamura[8], Toshikazu Onishi[10], Yasuo Fukui[11], Caroline Bot[12], Monica Rubio[13], Hajime Ezawa[4,8], Tai Oshima[4,14], Jason E. Austermann[15], Hiroshi Matsuo[4,14], Itziar Aretxaga[16], David H. Hughes[16], Ryohei Kawabe[17,4,18], Grant W. Wilson[19], and Min S. Yun[19]

[1] Institute of Astronomy, The University of Tokyo, 2-21-1 Osawa, Mitaka, Tokyo 181-0015, Japan
[2] Graduate School of Informatics and Engineering, The University of Electro-Communications, Chofu, Tokyo 182-8585, Japan
[3] Nobeyama Radio Observatory, National Astronomical Observatory of Japan (NAOJ), National Institutes of Natural Sciences (NINS), 462-2, Nobeyama, Minamimaki, Minamisaku, Nagano 384-1305, Japan
[4] Department of Astronomical Science, School of Physical Science, SOKENDAI (The Graduate University for Advanced Studies), 2-21-1, Osawa, Mitaka, Tokyo 181-8588, Japan
[5] Kogakuin University, 2665-1 Nakano, Hachioji, Tokyo 192-0015, Japan
[6] Joetsu University of Education, Joetsu, Niigata 943-8512, Japan
[7] Department of Physics, Faculty of Science, Hokkaido University, Sapporo 060-0810, Japan
[8] Chile Observatory, National Astronomical Observatory of Japan (NAOJ), National Institutes of Natural Sciences (NINS), 2-21-1, Osawa, Mitaka, Tokyo 181-8588, Japan
[9] Joint ALMA Observatory, Alonso de Córdova 3107, Vitacura, Santiago 763-0355, Chile
[10] Department of Physical Science, Osaka Prefecture University, Gakuen 1-1, Sakai, Osaka 599-8531, Japan
[11] Department of Astrophysics, Nagoya University, Chikusa-ku, Nagoya 464-8602, Japan
[12] Université de Strasbourg, CNRS, Observatoire astronomique de Strasbourg, UMR 7550, F-67000 Strasbourg, France
[13] Departamento de Astronomía, Universidad de Chile, Casilla 36-D, 8320000 Santiago, Chile
[14] Advanced Technology Center, National Astronomical Observatory (NAOJ), National Institutes of Natural Sciences (NINS), 2-21-1, Osawa, Mitaka, Tokyo 181-8588, Japan
[15] National Institute of Standards and Technology, Boulder, CO 80305, USA
[16] Instituto Nacional de Astrofísica, Óptica y Electrónica (INAOE), 72000 Puebla, Mexico
[17] National Astronomical Observatory of Japan (NAOJ), National Institutes of Natural Sciences (NINS), 2-21-1, Osawa, Mitaka, Tokyo 181-8588, Japan
[18] Department of Astronomy, School of Science, University of Tokyo, Bunkyo, Tokyo 133-0033, Japan
[19] Department of Astronomy, University of Massachusetts, Amherst, MA 01003, USA

Received 2017 December 9; revised 2018 September 22; accepted 2018 September 24; published 2018 November 6

Abstract

We present a high-sensitivity ($1\sigma < 1.6$ mJy beam^{-1}) continuum observation in a 343 arcmin^2 area of the northeast region of the Small Magellanic Cloud at a wavelength of 1.1 mm, conducted using the AzTEC instrument on the ASTE telescope. In the observed region, we identified 20 objects by contouring 10σ emission. Through spectral energy distribution analysis using 1.1 mm, *Herschel*, and *Spitzer* data, we estimated gas masses of 5×10^3–$7 \times 10^4\,M_\odot$, assuming a gas-to-dust ratio of 1000. The dust temperature and index of emissivity were also estimated as 18–33 K and 0.9–1.9, respectively, which are consistent with previous low-resolution studies. The dust temperature and the index of emissivity shows a weak negative linear correlation. We also investigated five CO-detected, dust-selected clouds in detail. The total gas masses were comparable to those estimated from the Mopra CO data, indicating that the assumed gas-to-dust ratio of 1000 and the $X_{\rm CO}$ factor of 1×10^{21} cm^{-2} (K km s^{-1})$^{-1}$, with uncertainties of a factor of 2, are reliable for the estimation of the gas masses of molecular or dust-selected clouds. The dust column density showed good spatial correlation with CO emission, except for an object associated with bright young stellar objects. The 8 μm filamentary and clumpy structures also showed a spatial distribution similar to that of the CO emission and dust column density, supporting the fact that polycyclic aromatic hydrocarbon emissions arise from the surfaces of dense gas and dust clouds.

Key words: galaxies: individual (SMC) – ISM: clouds – ISM: molecules – Magellanic Clouds

Supporting material: figure set

1. Introduction

The Small Magellanic Cloud (SMC) is a dwarf galaxy characterized by a metal-poor environment (Kurt et al. 1999; Larsen et al. 2000; Leroy et al. 2007; Planck Collaboration et al. 2011; Gordon et al. 2014) and active star formation (e.g., Vangioni-Flam et al. 1980; le Coarer et al. 1993; Bolatto et al. 2007). Because of its proximity (∼60 kpc; e.g., Hilditch et al. 2005) compared to other nearby galaxies, the SMC provides an invaluable opportunity to investigate the physics of the interstellar medium (ISM) and star formation, along with the Large Magellanic Cloud (LMC; e.g., Fukui & Kawamura 2010).

Previously, studies to unveil the star formation activity in the SMC were primarily motivated by the detection of giant molecular clouds (GMCs), which are the principal formation sites of stars (e.g., Israel et al. 1993, 2003; Rubio et al. 1993a, 1993b, 1996, 2000; Lequeux et al. 1994; Muller et al. 2003; Hony et al. 2015). The first GMC survey toward the full SMC was conducted by the Columbia Survey, where the detection of five GMCs, with masses of $\sim 10^6$–$10^7\,M_\odot$, at ∼160 pc resolution (Rubio et al. 1991), was reported. A subsequent

* *Herschel* is an ESA space observatory with science instruments provided by European-led Principal Investigator consortia and with important participation from NASA.

GMC survey at ∼50 pc resolution was conducted with the NANTEN 4 m telescope, and 21 GMCs, with masses of $\sim 10^4$–$10^6\,M_\odot$, were detected (Mizuno et al. 2001). High-resolution follow-up observations toward the NANTEN GMCs were also conducted using the Mopra telescope (Muller et al. 2010, 2013), resolving the NANTEN GMCs into compact (10^3–$10^4\,M_\odot$) molecular clumps. These studies pointed out that CO emission in the SMC is very weak, and the conversion factor, $X_{\rm CO} \simeq 10^{21}\,{\rm cm}^{-2}\ ({\rm K\,km\,s^{-1}})^{-1}$, is about 10 times larger than the typical value in the Milky Way galaxy. Recent numerical studies have suggested that the formation of molecules (H_2 and CO) in the low-metallicity ISM can occur later than the beginning of star formation (Glover & Clark 2012a, 2012b). These results imply that observations of CO lines are not always suitable for the detection of dense gas clouds that are connected to star formation in low-metallicity environments.

As a complementary approach to CO line observations, dust continuum emission can also be a good tracer of dense gas clouds via the thermal emission from cold dust. Toward the SMC southwest (SW) region, observations by SEST/SIMBA at 1.2 mm (Rubio et al. 2004; Bot et al. 2007) and APEX/LABOCA at 870 μm succeeded in detecting the CO clouds (Bot et al. 2010a). N66 has also been investigated in detail using LABOCA and *Herschel* by Hony et al. (2015). Recently, Takekoshi et al. (2017) attempted a new cloud identification method using 1.1 mm continuum survey data toward the full SMC obtained by AzTEC on ASTE. They identified 44 dust-selected cloud samples in the full SMC with a gas mass range of 4×10^3–$3 \times 10^5\,M_\odot$. This survey also discovered dust-selected clouds not associated with CO lines or star formation activity; these objects are expected to be rare samples of the youngest evolution phase of GMCs in the SMC.

Takekoshi et al. (2017), however, did not report the detection of the two CO clouds discovered by NANTEN in the northeast (NE) region. These objects are characterized by relatively weak star formation activity compared to the other GMCs in the SMC. This suggests that these clouds have a low dust temperature or low surface brightness, which is not sufficient to detect the peak flux because of the inadequate survey sensitivity. Thus, it is important to observe these objects using the 1.1 mm continuum with high-sensitivity observations.

In this paper, we present the results of a 1.1 mm deep observation toward the SMC NE region in order to reveal the hidden aspects of GMCs in low-metallicity ISM using dust, CO, and star formation tracers. In Section 2, the observation and reduction of the AzTEC and *Herschel* data are described. In Section 3, we present the multiwavelength images and catalog of 1.1 mm objects. Section 4 describes the method of spectral energy distribution (SED) analysis using both object- and image-based approaches. The statistical properties of the low-mass, dust-selected clouds in the NE region are discussed in Section 5. The relationship among the distribution of dust, CO, and star formation activity is discussed with the result of the image-based SED fitting toward the NANTEN GMCs in Section 6. Finally, we summarize the results of this study in Section 7.

2. Observation and Data Sets

2.1. AzTEC/ASTE Observation

Observations of the 1.1 mm continuum toward the SMC NE region were conducted with the AzTEC instrument (Wilson et al. 2008a) mounted on the ASTE 10 m telescope (Ezawa et al. 2004, 2008) on 2007 August 28–31 and October 4–6, and 2008 August 28–30. The observation region is shown in Figure 1. The zenith opacity at 220 GHz was in the range of 0.01–0.16, and the median was 0.06. The total observing time was about 20 hr. The observations were performed by $16' \times 16'$ and $10' \times 10'$ Lissajous scans with a peak velocity of $330''\,{\rm s}^{-1}$. Pointing observations toward quasar J0047–579 or 2355–534 were observed every 1.5 hr, and the accuracy was better than 3″ rms (Wilson et al. 2008b). The uncertainty of the flux calibration with Uranus was 8% (Wilson et al. 2008b; Liu et al. 2010).

Data reduction was performed with the FRUIT method, which is an iterative principal component analysis cleaning method (Scott et al. 2008; Liu et al. 2010; Downes et al. 2012), to recover extended emission. The FRUIT method effectively removes atmospheric emission, which is a dominant noise source in ground-based continuum observation, extended over the field of view of the instrument and correlated with the bolometer pixels. At the same time, widely extended astronomical signals, which are also correlated with the bolometer pixels, are also removed. Simulations of the reproducibility of extended sources using Gaussian model sources show that >60% of the total flux density and ∼100% of the peak flux density are recovered for compact objects smaller than 3′ FWHM in our cases, which corresponds to the typical size of the detected objects in the observation region, as shown in Section 3 (Komugi et al. 2011; Shimajiri et al. 2011; Takekoshi et al. 2017).

As a result of the FRUIT method, the minimum and median noise levels achieved were 1.16 and 1.31 mJy beam^{-1}, respectively. The total area better than 1.64 mJy beam^{-1}, which is $\sqrt{2}\times$ the minimum noise level and used for further data analysis in this paper, was 343.4 arcmin^2 (roughly $20' \times 20'$). The FWHM of the point response function (PRF) after the FRUIT procedure was 40″, which corresponds to 12 pc. FRUIT also added an uncertainty of 10% to the photometry of the detected objects (Takekoshi et al. 2017). The total photometric accuracy was estimated to be 13% from the root sum square of the flux calibration and FRUIT photometric accuracy.

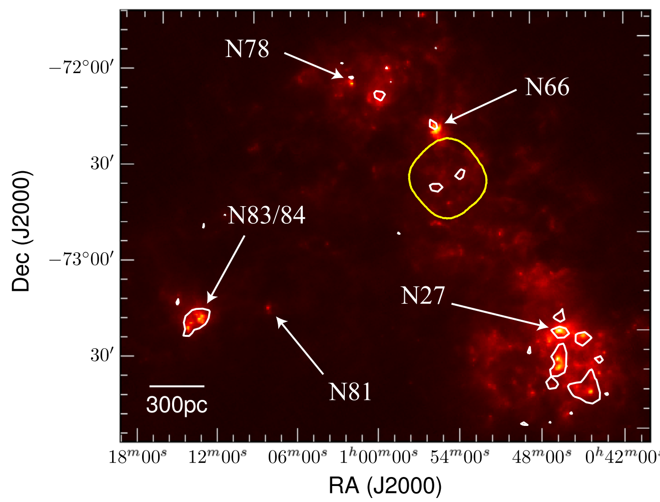

Figure 1. *Spitzer* 160 μm image of the SMC. The observation regions of AzTEC/ASTE are represented by the yellow outline. The white contours represent the NANTEN CO intensity (0.5 K km s^{-1}).

2.2. Herschel *Data*

We used the *Herschel*/PACS (100 and 160 μm) and SPIRE (250, 350, and 500 μm) data (Meixner et al. 2013; Gordon et al. 2014) to estimate the amount and property of the cold dust component. Some part of the extended component of the 1.1 mm data analyzed by the FRUIT procedure, which is removed as correlated noise similar to atmospheric emission, is lost. In order to compare with the 1.1 mm data directly, the FRUIT procedure was applied to the *Herschel* images in the same manner as in Takekoshi et al. (2017). After the FRUIT procedure, the FWHM of the PRF was 40″. The image noise levels after the FRUIT analysis were 383, 213, 25.6, 12.8, and 8.5 mJy beam^{-1} for the *Herschel* 100, 160, 250, 350, and 500 μm data, respectively. We also considered the propagation of the 1.1 mm image noise that was caused by the FRUIT analysis. The photometric errors of the *Herschel* data after the FRUIT analysis was 14% and 13% for the PACS and SPIRE data, respectively, which was estimated from the root sum square of the calibration accuracy (8% and 10% for SPIRE and PACS data, respectively) and additional error from the FRUIT analysis (10%; Takekoshi et al. 2017).

2.3. Molecular Gas and Star Formation Tracers

We used the CO ($J = 1 - 0$) data obtained by the Mopra telescope (MAGMA-SMC; Muller et al. 2010, 2013). The observation was made toward the GMCs detected by the NANTEN survey (Mizuno et al. 2001). The spatial resolution was 33″ FWHM with a sensitivity of about 150 mK and velocity resolution binned to 0.35 km s^{-1}. In the observation region of the AzTEC 1.1 mm continuum, Muller et al. (2010) reported the detection of four CO clumps in this region, which have gas masses of 10^3–$10^4\,M_\odot$ assuming $X_{\rm CO} = 1 \times 10^{21}$ cm^{-1} (K km s^{-1})$^{-1}$.

In order to investigate the star formation activity, we used the *Spitzer*/IRAC 8 μm and MIPS 24 and 70 μm data (Gordon et al. 2011). We did not apply FRUIT analysis, as the spatial distributions differed greatly from those in the AzTEC and *Herschel* data because of the tracing of different dust components (very small grains or polycyclic aromatic hydrocarbons (PAHs)). The noise levels and photometric accuracy were 0.02, 0.06, and 0.5 MJy sr^{-1}, and 5%, 4%, and 5% for 8, 24, and 70 μm, respectively. We also used the *Spitzer* young stellar object (YSO) catalogs provided by Bolatto et al. (2007) and Sewiło et al. (2013) to determine whether star formation activity is associated. In addition, we compared with the Hα data obtained by the Magellanic Cloud Emission-Line Survey project (Smith et al. 2000) and with the radio continuum data at 8.64 and 4.8 GHz (ATCA and Parkes; Dickel et al. 2010) as another tracer of star-forming regions.

3. Results

3.1. Maps

Figure 2 shows the continuum emission at AzTEC 1.1 mm, *Herschel* 100–500 μm, and *Spitzer* 8, 24, and 70 μm in the observation region. We did not subtract free–free emissions from the maps, because the observed region shows no strong radio continuum emission. The 1.1 mm emission over 5σ shows good spatial correlation with the *Herschel* images. This indicates that the AzTEC and *Herschel* bands trace a cold dust component. In contrast, the images at shorter wavelengths exhibit a compact spatial distribution because these bands efficiently trace thermal dust emission from hotter and more compact star formation activity (e.g., Bolatto et al. 2007; Leroy et al. 2007). All CO clouds discovered by NANTEN and Mopra in this region were detected over 10σ in the 1.1 mm image, which we will discuss in Section 6.

3.2. The 1.1 mm Object Catalog

The 1.1 mm objects (hereafter called NEdeep objects) were identified by contouring over the 10σ emission in the 1.1 mm image. As a result, 20 objects, listed in Table 1, were identified in the observing area. Out of the detected objects, three objects were detected on the edge of the 1.1 mm image. We did not use these objects for statistical analysis in Section 5. In the same manner as Takekoshi et al. (2017), the 1.1 mm objects were classified by whether star formation tracers such as H II regions, YSO candidates, or bright 24 μm sources (>10 MJy sr^{-1}) exist in the objects. As a result, we identified eight objects exhibiting star formation activity, and some of them are compact and faint at 1.1 mm, such as NEdeep-15 and 18. Therefore, the 1.1 mm objects are good candidates for dense gas clouds that are likely to form massive stars.

The spatial distribution of the identified NEdeep objects is presented in Figure 3. The NANTEN objects at the eastern and western sides consist of two and three compact NEdeep objects, respectively. NEdeep-1 and 3, located at the northeast edge, are continuously connected to the N66 star-forming region. The compact objects at the western side seem to be packed into some small regions and could be associated with each other. In contrast, NEdeep-2, 6, 11, 14, 15, and 20 seem to exist as independent compact objects.

4. SED Analysis

As shown in Figure 2, the 1.1 mm emission shows a reasonable spatial correlation to the *Herschel* 100–500 μm emission. This indicates that these bands are emitted by the cold dust component that dominates the total dust mass. In order to estimate the dust temperature and dust mass of the identified 1.1 mm objects, SED analysis was performed using the 1.1 mm and *Herschel* 100, 160, 250, 350, and 500 μm data assuming a single dust temperature. We also used the photometry of *Spitzer* 24 and 70 μm as upper limits. Table 2 shows flux densities estimated from the data sets to use the SED fit. The total flux density of cold thermal dust emission at the wavelength λ, $S_{{\rm obs},\lambda}$, can be modeled by

$$S_{{\rm model},\lambda} = \kappa_{{\rm dust},\lambda} B_\lambda(T_{\rm dust}) M_{\rm dust} D^{-2}, \tag{1}$$

where $\kappa_{{\rm dust},\lambda}$ is the emissivity of dust grains, B_λ is the Planck function, $M_{\rm dust}$ is the total dust mass, $T_{\rm dust}$ is the dust temperature, and $D = 60$ kpc is the distance to the SMC (e.g., Hilditch et al. 2005). For the emissivity of the cold dust component, we used $\kappa_{{\rm dust},\lambda} = 12.5 \times (160\,\mu{\rm m}/\lambda)^\beta$ cm^2 g^{-1} (Draine & Li 2007; Draine et al. 2014). We estimated the posterior distributions of $T_{\rm dust}$, $M_{\rm dust}$, and the index of emissivity β using the Markov Chain Monte Carlo (MCMC) method. The likelihood function is defined as

$$L = \prod_\lambda L_\lambda, \tag{2}$$

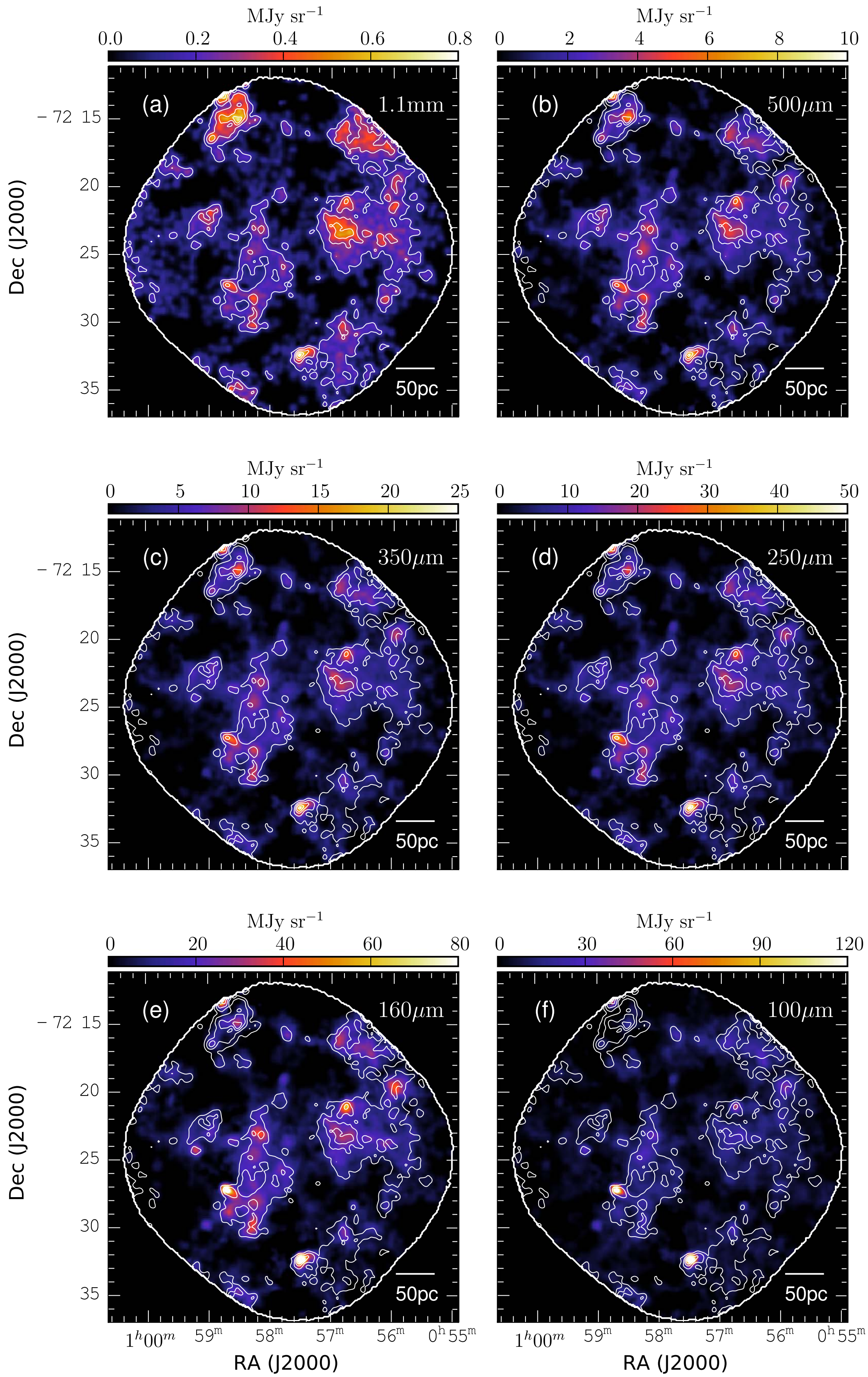

Figure 2. Multiband continuum images of the SMC NE region. The white contours represent the 1.1 mm image, starting from 6.5 mJy beam^{-1} ($\sim 5\sigma$) with a step of 6.5 mJy beam^{-1}. (a) AzTEC/ASTE 1.1 mm. (b) *Herschel*/SPIRE 500 μm. (c) *Herschel*/SPIRE 350 μm. (d) *Herschel*/SPIRE 250 μm. (e) *Herschel*/PACS 160 μm. (f) *Herschel*/PACS 100 μm. (g) *Spitzer*/MIPS 70 μm. (h) *Spitzer*/MIPS 24 μm. (i) *Spitzer*/IRAC 8 μm. The edge of the 1.1 mm image is also indicated by the white contour.

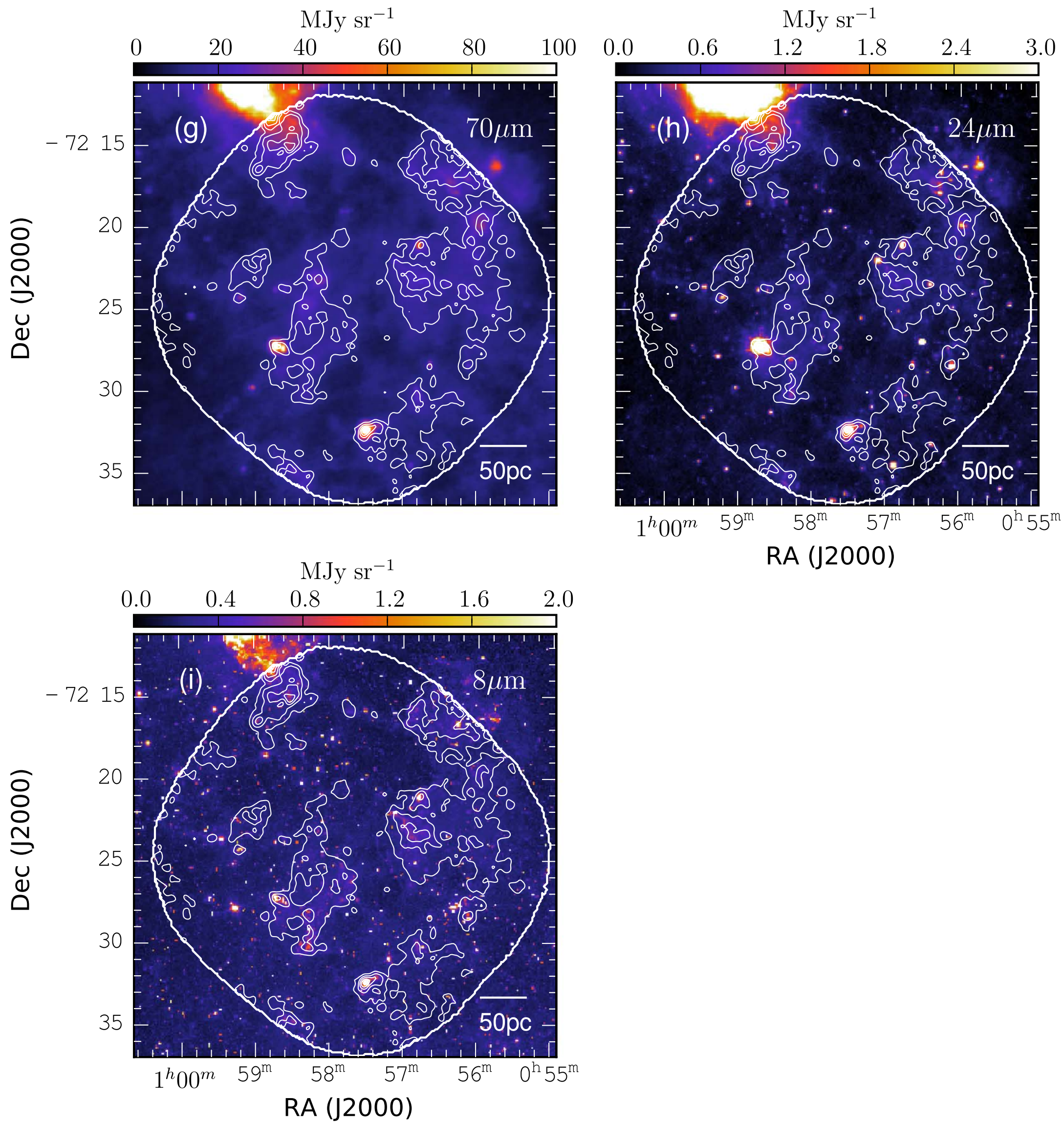

Figure 2. (Continued.)

and

$$L_\lambda = \exp\left(-\frac{(S_{\rm obs,\lambda} - S_{\rm mod,\lambda})^2}{2\sigma^2_{\rm obs,\lambda}}\right). \tag{3}$$

For the upper limits of photometry, we used the one-sided Gaussian distribution:

$$L_\lambda \propto \begin{cases} 1 & (0 \leqslant S_{\rm model,\lambda} \leqslant S_{\lambda,\rm obs}) \\ \exp\left(-\frac{(S_{\rm obs,\lambda} - S_{\rm mod,\lambda})^2}{2\sigma^2_{\rm obs,\lambda}}\right) & (S_{\rm model,\lambda} > S_{\rm obs,\lambda}) \end{cases}. \tag{4}$$

We assumed uniform prior probability distributions for the fitting parameters, with the ranges of $0 < T_{\rm dust}({\rm K}) < 60$, $0 < \log(M_{\rm dust}/M_\odot) < 4$, and $0 < \beta < 5$. We used `PyMC3` (Salvatier et al. 2016) to implement the MCMC method.

By selecting a previously known gas-to-dust ratio GDR = 1000 (with a possible error of a factor of 2, Leroy et al. 2007; Planck Collaboration et al. 2011; Gordon et al. 2014; Roman-Duval et al. 2014), the total gas masses $M_{\rm gas}$ were estimated by

$$M_{\rm gas} = {\rm GDR} \times M_{\rm dust}. \tag{5}$$

The SEDs of the 1.1 mm objects are presented in Figure 4, and the obtained physical properties are summarized in Table 3.

In Section 6, we also attempted an image-based SED fit to discuss the detailed structures of the detected clumps. Using the same posterior distributions of the dust temperature and index of dust emissivity, and the uniform posterior for the column density of cold dust $N_{\rm dust}$ in the range of $-10 < \log(N_{\rm dust}/({\rm g\,cm^{-2}})) < -3$, we estimate the parameters using the following equation:

$$I_\lambda = \kappa_{\rm dust,\lambda} B_\lambda(T_{\rm dust}) N_{\rm dust}, \tag{6}$$

where I_λ is the flux density of each pixel.

We should pay attention to the possibility of a larger $\kappa_{\rm dust,\lambda}$. In the SMC and LMC, Gordon et al. (2017) suggested that $\kappa_{\rm dust,160\,\mu m} = 30.2\,{\rm cm^2\,g^{-1}}$, which is about three times larger than that of some physically motivated models (e.g.,

Table 1
AzTEC/ASTE 1.1 mm Extended Source Catalog of the SMC NE Region

Object ID	α ($J2000$)	δ ($J2000$)	1.1 mm Peak Flux (mJy beam^{-1})	S/N	1.1 mm Total Flux (mJy)	R (pc)	Star Formation?	Map Edge?
NEdeep-1	$00^{\mathrm{h}}58^{\mathrm{m}}45\overset{\mathrm{s}}{.}9$	$-72^\circ13'18''$	48.7 ± 2.3	21.0	28.8 ± 4.1	8.0	Yes	Yes
2	$00^{\mathrm{h}}57^{\mathrm{m}}30\overset{\mathrm{s}}{.}7$	$-72^\circ32'30''$	34.1 ± 1.3	27.2	42.5 ± 5.5	10.2	Yes	No
3	$00^{\mathrm{h}}58^{\mathrm{m}}31\overset{\mathrm{s}}{.}5$	$-72^\circ15'12''$	31.6 ± 1.5	21.5	191.1 ± 24.5	22.9	No	No
4	$00^{\mathrm{h}}56^{\mathrm{m}}42\overset{\mathrm{s}}{.}0$	$-72^\circ23'29''$	24.4 ± 1.2	20.2	142.0 ± 18.2	20.0	Yes	No
5	$00^{\mathrm{h}}56^{\mathrm{m}}46\overset{\mathrm{s}}{.}1$	$-72^\circ21'05''$	21.9 ± 1.2	18.0	27.1 ± 3.6	9.2	Yes	No
6	$00^{\mathrm{h}}58^{\mathrm{m}}38\overset{\mathrm{s}}{.}8$	$-72^\circ35'00''$	21.5 ± 2.2	9.6	10.4 ± 2.6	5.8	No	Yes
7	$00^{\mathrm{h}}58^{\mathrm{m}}41\overset{\mathrm{s}}{.}1$	$-72^\circ27'18''$	21.3 ± 1.2	17.6	19.3 ± 2.6	7.6	Yes	No
8	$00^{\mathrm{h}}56^{\mathrm{m}}54\overset{\mathrm{s}}{.}3$	$-72^\circ16'35''$	21.2 ± 1.7	12.5	156.6 ± 20.1	22.6	Yes	Yes
9	$00^{\mathrm{h}}58^{\mathrm{m}}17\overset{\mathrm{s}}{.}3$	$-72^\circ28'18''$	18.6 ± 1.2	15.0	11.6 ± 1.9	6.1	No	No
10	$00^{\mathrm{h}}55^{\mathrm{m}}59\overset{\mathrm{s}}{.}9$	$-72^\circ21'34''$	18.3 ± 1.3	13.8	12.3 ± 2.0	6.2	No	No
11	$00^{\mathrm{h}}58^{\mathrm{m}}58\overset{\mathrm{s}}{.}1$	$-72^\circ21'59''$	17.4 ± 1.2	14.3	20.1 ± 2.7	8.3	No	No
12	$00^{\mathrm{h}}56^{\mathrm{m}}12\overset{\mathrm{s}}{.}9$	$-72^\circ23'46''$	17.1 ± 1.2	13.9	12.7 ± 2.0	6.5	No	No
13	$00^{\mathrm{h}}58^{\mathrm{m}}17\overset{\mathrm{s}}{.}3$	$-72^\circ30'18''$	16.9 ± 1.3	13.4	16.7 ± 2.3	7.6	No	No
14	$00^{\mathrm{h}}56^{\mathrm{m}}49\overset{\mathrm{s}}{.}5$	$-72^\circ30'23''$	16.6 ± 1.3	13.1	14.4 ± 2.1	7.1	No	No
15	$00^{\mathrm{h}}56^{\mathrm{m}}07\overset{\mathrm{s}}{.}1$	$-72^\circ28'22''$	16.6 ± 1.3	12.4	7.6 ± 1.8	5.0	Yes	No
16	$00^{\mathrm{h}}56^{\mathrm{m}}03\overset{\mathrm{s}}{.}6$	$-72^\circ23'46''$	16.0 ± 1.2	12.8	10.2 ± 1.8	5.9	No	No
17	$00^{\mathrm{h}}56^{\mathrm{m}}05\overset{\mathrm{s}}{.}2$	$-72^\circ20'52''$	15.9 ± 1.3	11.9	<4.9 ± 2.0	4.1	No	No
18	$00^{\mathrm{h}}56^{\mathrm{m}}26\overset{\mathrm{s}}{.}1$	$-72^\circ23'29''$	15.8 ± 1.2	13.0	7.7 ± 1.7	5.1	Yes	No
19	$00^{\mathrm{h}}56^{\mathrm{m}}00\overset{\mathrm{s}}{.}1$	$-72^\circ19'58''$	15.4 ± 1.4	10.8	14.8 ± 2.2	7.2	No	No
20	$00^{\mathrm{h}}58^{\mathrm{m}}07\overset{\mathrm{s}}{.}9$	$-72^\circ23'06''$	15.0 ± 1.2	12.6	<5.0 ± 1.8	4.2	No	No

Note. The columns give the (1) source ID, (2) R.A., (3) decl., (4) observed peak flux and noise level at 1.1 mm, (5) signal-to-noise ratio, (6) 1.1 mm total flux, (7) source radius, (8) whether the object is associated with YSOs or 24 μm objects, and (9) whether or not the object is located at the map edge.

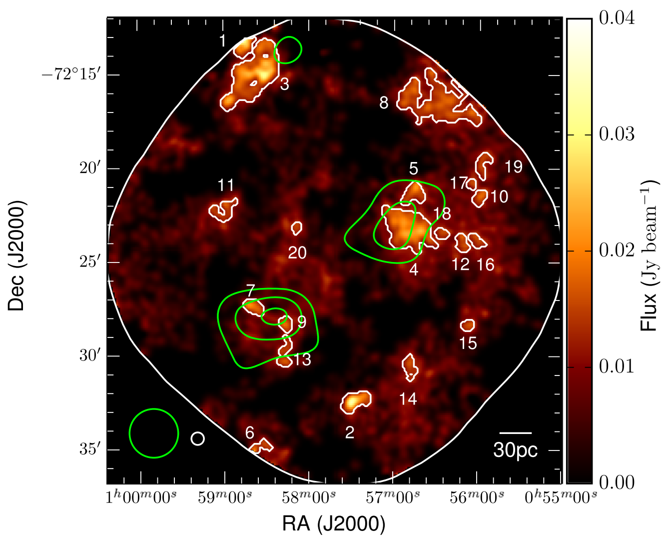

Figure 3. The 1.1 mm image of the SMC NE region. The identified dust-selected clouds are shown by the white contours. The green contours represent the NANTEN CO intensity with a step of 0.3 K km s^{-1} starting from 0.3 K km s^{-1}. The numbers represent the object IDs. The circles at the bottom-left corner represent the effective resolutions of AzTEC/ASTE 1.1 mm (white) and NANTEN CO (green).

Draine & Li 2007). This causes a dust mass estimate about three times lower than our $\kappa_{\mathrm{dust},\lambda}$ value.

5. Physical Properties of NEdeep Objects

5.1. Comparison with Wide-survey Objects

The 1.1 mm objects identified by Takekoshi et al. (2017; hereafter wide-survey objects) are potential candidates for dense gas clouds that are forming or about to form massive stars. In the wide-survey objects, only NE-1 was detected as a counterpart of the NEdeep-1 object in the NE field. The sensitivity of the wide survey is about 6 mJy beam^{-1} in this region, which is not sufficient to detect the other NEdeep objects with $>5\sigma$. Thus, the high-sensitivity NEdeep observations provide information about many objects that are undetectable in the wide survey.

Table 4 presents the typical physical properties of the NEdeep and wide-survey objects. We included neither the three objects in the NEdeep samples located at the edge of the 1.1 mm images nor N88-1 of the wide-survey objects in the statistics. Takekoshi et al. (2017) assumed a fixed $\beta = 1.2$ for estimating the dust temperature and mass of the wide-survey objects. Here, we estimated the average and standard deviation values of $\beta = 1.3 \pm 0.3$ for the NEdeep objects, and this difference between the free β and $\beta = 1.2$ fits causes systematic average differences of 5% and 8% for the dust temperature and mass (except for upper-limit values) estimate, respectively. Thus, roughly speaking, the physical properties of wide-survey and NEdeep objects are able to be compared directly.

Comparing the wide-survey and NEdeep objects shows that the statistical physical properties of the NEdeep objects, other than the mass and size, are roughly consistent with those of the wide-survey objects. By contrast, the mass and size of the NEdeep objects are relatively smaller than those of the wide-survey objects, which indicates that the high-sensitivity observation makes it possible to detect lower mass objects. These low-mass objects are also good candidates for dense gas clumps that are connected to massive star formation, because about 40% of the NEdeep objects host YSOs, including lower mass objects, such as NEdeep-15 and 18.

The dust temperature of the NEdeep objects may be slightly lower than that of the wide-survey objects. The difference in star-forming activity between the NEdeep and wide-survey objects could explain this difference, because the wide-survey objects include very active star-forming regions such as Lirs49, SMCB-2N, and N66, which have the dust temperature of

Table 2
Total Flux Densities of the 1.1 mm Extended Objects

Object ID	$S_{1.1\ \mathrm{mm}}$ (mJy)	$S_{Herschel 500\ \mu\mathrm{m}}$ (mJy)	$S_{Herschel 350\ \mu\mathrm{m}}$ (mJy)	$S_{Herschel 250\ \mu\mathrm{m}}$ (mJy)	$S_{Herschel 160\ \mu\mathrm{m}}$ (mJy)	$S_{Herschel 100\ \mu\mathrm{m}}$ (mJy)	$S_{Spitzer 70\ \mu\mathrm{m}}$ (mJy)	$S_{Spitzer 24\ \mu\mathrm{m}}$ (mJy)
NEdeep-1	28.77 ± 4.05	219.57 ± 29.21	499.99 ± 42.50	865.16 ± 74.42	1348.15 ± 209.14	<880.38 + 294.55	<3429.12 + 172.15	<117.67 + 5.06
2	42.50 ± 5.49	458.14 ± 58.91	1133.80 ± 145.45	2396.13 ± 307.31	5457.49 ± 781.40	7256.19 ± 1049.08	<5666.17 + 283.57	<584.42 + 23.42
3	191.15 ± 24.48	1290.85 ± 165.33	2804.53 ± 224.40	4315.19 ± 345.31	5355.56 ± 538.37	1929.04 ± 216.38	<14249.72 + 712.51	<393.60 + 15.76
4	142.01 ± 18.19	1233.59 ± 158.00	2746.50 ± 219.76	5144.05 ± 411.61	8448.07 ± 847.12	6929.23 ± 701.90	<7295.19 + 364.81	<186.96 + 7.52
5	27.14 ± 3.56	313.51 ± 40.57	735.53 ± 59.61	1442.02 ± 116.86	2785.09 ± 310.21	1846.36 ± 306.06	<1739.19 + 88.00	<59.43 + 2.88
6	10.37 ± 2.60	76.10 ± 14.50	172.45 ± 23.76	326.48 ± 45.17	<564.61 + 226.32	<503.26 + 389.14	<595.94 + 36.61	<12.50 + 2.61
7	19.29 ± 2.64	244.03 ± 32.04	635.78 ± 52.16	1433.03 ± 116.86	3179.00 ± 358.57	4056.86 ± 502.43	<3113.91 + 156.56	<1232.81 + 49.35
8	156.64 ± 20.06	1205.48 ± 154.40	2654.83 ± 212.43	4927.65 ± 394.30	8909.95 ± 892.75	7685.05 ± 774.90	<9161.29 + 458.10	<223.78 + 8.98
9	11.58 ± 1.90	141.30 ± 20.15	314.92 ± 29.08	569.66 ± 53.67	948.30 ± 227.46	<650.74 + 375.03	<635.30 + 37.76	<19.94 + 2.58
10	12.29 ± 2.00	96.39 ± 15.13	185.58 ± 20.72	316.58 ± 37.88	<480.18 + 207.40	<597.94 + 364.99	<695.84 + 40.08	<14.18 + 2.46
11	20.06 ± 2.71	180.47 ± 24.00	361.14 ± 30.77	580.18 ± 50.81	750.48 ± 168.82	<577.87 + 276.31	<923.12 + 48.51	<17.41 + 1.93
12	12.67 ± 1.96	81.42 ± 13.34	192.31 ± 20.55	355.29 ± 38.94	766.82 ± 208.93	<517.02 + 351.03	<734.78 + 41.45	<15.37 + 2.39
13	16.67 ± 2.34	193.16 ± 25.74	466.69 ± 39.13	893.76 ± 75.06	1612.17 ± 231.38	1064.76 ± 314.97	<884.74 + 47.17	<26.68 + 2.24
14	14.44 ± 2.12	133.41 ± 18.70	284.63 ± 25.97	524.53 ± 48.53	910.94 ± 198.90	<835.20 + 326.61	<903.96 + 48.45	<19.09 + 2.23
15	7.59 ± 1.83	62.01 ± 13.45	128.06 ± 20.69	227.14 ± 39.44	<321.88 + 252.35	<296.14 + 447.59	<341.51 + 30.01	<32.78 + 3.24
16	10.19 ± 1.79	76.26 ± 13.36	166.25 ± 20.01	302.98 ± 37.95	<600.05 + 220.76	<360.79 + 381.19	<589.28 + 36.17	<11.29 + 2.56
17	<4.91 + 2.02	<31.78 + 14.03	73.52 ± 22.99	<133.06 + 44.58	<246.95 + 310.52	<265.75 + 552.96	<324.77 + 34.57	<6.95 + 3.68
18	7.68 ± 1.69	54.02 ± 12.56	127.18 ± 19.93	232.85 ± 38.32	<503.19 + 250.32	<446.56 + 440.42	<466.29 + 33.62	<18.65 + 3.00
19	14.80 ± 2.22	160.25 ± 21.92	379.77 ± 32.98	741.74 ± 64.37	1578.41 ± 236.04	1417.27 ± 343.46	<1262.21 + 65.43	<33.48 + 2.47
20	<5.02 + 1.79	67.04 ± 15.42	150.84 ± 24.14	284.33 ± 46.78	<579.83 + 305.80	<482.72 + 538.76	<405.30 + 35.92	<7.53 + 3.58

Note. The two values provided in each cell show the representative fluxes and 1σ errors. We indicate the upper-limit values for the combination of the uniform and normal distributions in the MCMC analysis by "<."

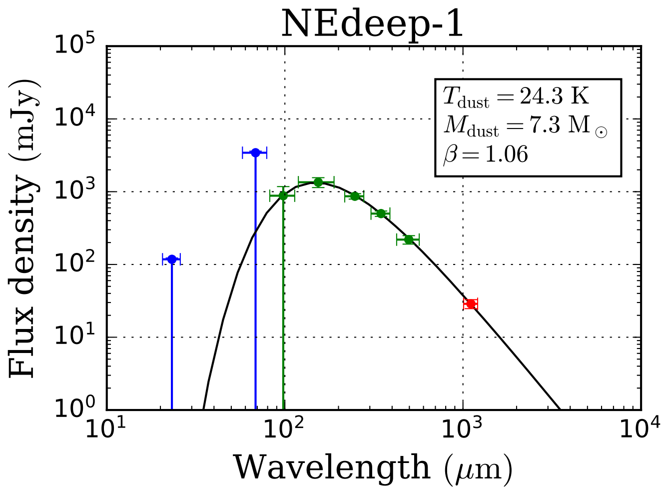

Figure 4. SEDs of the AzTEC/SMC NEdeep objects. The solid line represents the maximum likelihood SED models for the cold dust component. The red (1.1 mm), green (*Herschel* 100, 160, 250, 350, and 500 μm), and blue (*Spitzer* 24 and 70 μm) points represent the fitting points for the cold dust SED. The fitting parameters of the maximum likelihood model are shown in each figure.

(The complete figure set (20 images) is available.)

$\sim$40 K (Takekoshi et al. 2017). We avoid further discussion of the comparison with the wide-survey objects here, because of the difference with the SED fit models.

The area in the SMC NE region observed is only about 2% that of the wide field, and therefore, a more sensitive ($\sim$1 mJy rms) and wider (a few square degrees) survey of the SMC at 1.1 mm will provide several hundred samples of dust-selected clouds, down to a gas mass of $1 \times 10^3 M_\odot$. It is also important for high-resolution observations to detect gas clumps of $<10^3 M_\odot$, because the sizes of many NEdeep objects are very close to the diffraction limit.

5.2. Index of Emissivity and the β–T$_{dust}$ Relation

Here, we investigate the characteristics of the index of emissivity in detail. First, as shown in Tables 3 and 4, the range of β is 0.9–1.9. This is consistent with the reasonable range of single-temperature dust particles, $1 < \beta < 2$, motivated by the Kramers–Kronig relation at long wavelengths and the emissivity model for silicates (e.g., Draine & Lee 1984).

Second, previous studies, using lower resolution data sets, show $\beta \sim 1.2$ in the SMC (Aguirre et al. 2003; Leroy et al. 2007; Bot et al. 2010b; Israel et al. 2010; Planck Collaboration et al. 2011). The average ($\pm$ standard deviation) value obtained, $\beta_{\rm ave.} = 1.3 \pm 0.3$, in the NEdeep objects is consistent with these studies. On the other hand, the wide range of β values among the NEdeep objects suggests that the existence of a complex temperature structure or difference in dust composition affects the index of emissivity of each dust-selected cloud.

Finally, the relation between dust temperature and index of emissivity is shown in Figure 5. As a result of fitting with a linear function, we obtained the relationship

$$\beta(T_{\rm dust}) = (-0.03 \pm 0.01) T_{\rm dust} + (1.93 \pm 0.34). \quad (7)$$

The negative correlation of the β–$T_{\rm dust}$ relation has already been reported by Gordon et al. (2014) in the SMC using the pixel-based SED fit with the minimum χ^2 method. Some studies revealed that the minimum χ^2 method is very susceptible to data noise and gives rise to the negative β–$T_{\rm dust}$ relation (e.g., Shetty et al. 2009a, 2009b). On the other hand, the MCMC method can significantly reduce the noise-induced β–$T_{\rm dust}$ correlations (Kelly et al. 2012; Juvela et al. 2013). Thus, our result suggests that the negative β–$T_{\rm dust}$ relation in NEdeep objects is intrinsic, and its origin can be attributed to the difference in physical structures or dust properties.

Some possible interpretations of the negative β–$T_{\rm dust}$ relation have been proposed by model and simulation studies of molecular cores (e.g., Shetty et al. 2009a; Malinen et al. 2011; Juvela & Ysard 2012). The difference in the line-of-sight temperature structures of dust-selected clouds, particularly internally heated objects, creates a negative β–$T_{\rm dust}$ relation. Although this picture is consistent with the dust temperature and *Spitzer* 24 μm relation, which supports the fact that the heating source of dust-selected clouds is mainly local star formation activity (Takekoshi et al. 2017), we cannot find a clear relation with the existence of star formation activity in the β–$T_{\rm dust}$ relation, as shown in Figure 5. On the other hand, the photometric errors and band selections also cause a weak negative or positive bias, even in the case of the MCMC fit. Further investigation using analytic or simulation modeling, and larger and more sensitive observation of dust-selected clouds, is necessary to reveal the origin of the β–$T_{\rm dust}$ relation.

6. Comparison with CO Emission and Star Formation Tracer

The 1.1 mm objects already detected by the NANTEN and Mopra CO observations in the observation region exhibit weaker star formation activity than the other CO-selected molecular clouds in the SMC. Therefore, these objects might remain at the initial state of molecular cloud evolution without the influence of star formation. Thus, these 1.1 mm objects are very important to understand the relationship between the chemical and dynamical evolution of molecular clouds in the low-metallicity environment.

In this section, we reveal the characteristics of the molecular clouds that already have reported CO detection (Mizuno et al. 2001; Muller et al. 2010) by comparing the gas mass obtained from the CO data and the distribution of YSOs. In addition, we investigate the internal structure of these objects by comparing the CO and PAH distributions and the result of the map-based SED analysis of dust continuum data.

6.1. Gas Mass Estimate from CO

The gas masses estimated from the SED fit of the thermal dust continuum are not taken into consideration because of the possible bias caused by the gas-to-dust ratio, emissivity, and temperature distributions in the objects. Therefore, it is important to compare the gas masses estimated from the CO luminosity as another tracer of gas mass to check for consistency. We estimated the gas masses of the NEdeep-4, 5, 7, 9, and 13 objects using the Mopra CO data assuming an $X_{\rm CO}$ factor with the following steps. First, we estimated the CO luminosity within the contours of the 1.1 mm objects and velocity range of the CO line. Second, we estimated the gas masses using the following equation:

$$M_{\rm gas,CO}(M_\odot) = 2\,\mu m_{\rm p} X_{\rm CO} L_{\rm CO} \quad (8)$$

$$= 21.8\, L_{\rm CO}({\rm K\ km\ s^{-1}\ pc^2}), \quad (9)$$

Table 3
Physical Properties of the 1.1 mm Extended Objects

Object ID	T_{dust} (K)	M_{dust} ($M_\odot$)	M_{gas} ($\times 10^3 M_\odot$)	β	n_{H_2} (H_2/cm^3)	N_{H_2} ($\times 10^{20} H_2/cm^2$)
NEdeep-1	24.3 ± 2.3	<8.6	<8.6	1.06 ± 0.14	<180.0	<59.2
2	33.0 ± 2.3	$10.7^{+2.8}_{-2.2}$	$10.7^{+2.8}_{-2.2}$	1.24 ± 0.11	$35.7^{+9.3}_{-7.4}$	$15.0^{+3.9}_{-3.1}$
3	19.5 ± 0.7	$70.4^{+14.1}_{-11.7}$	$70.4^{+14.1}_{-11.7}$	1.12 ± 0.11	$21.0^{+4.2}_{-3.5}$	$19.8^{+4.0}_{-3.3}$
4	26.3 ± 1.3	$35.2^{+7.2}_{-6.0}$	$35.2^{+7.2}_{-6.0}$	1.09 ± 0.10	$15.7^{+3.2}_{-2.7}$	$12.9^{+2.6}_{-2.2}$
5	23.4 ± 1.2	$16.3^{+3.7}_{-3.0}$	$16.3^{+3.7}_{-3.0}$	1.47 ± 0.11	$75.1^{+17.2}_{-14.0}$	$28.4^{+6.5}_{-5.3}$
6	25.2 ± 5.5	<9.7	<9.7	1.12 ± 0.31	<529.1	<126.8
7	30.1 ± 1.8	$8.4^{+1.9}_{-1.5}$	$8.4^{+1.9}_{-1.5}$	1.46 ± 0.10	$69.6^{+15.6}_{-12.7}$	$21.7^{+4.9}_{-4.0}$
8	29.1 ± 1.6	$25.1^{+5.3}_{-4.4}$	$25.1^{+5.3}_{-4.4}$	0.93 ± 0.10	$7.8^{+1.7}_{-1.4}$	$7.2^{+1.5}_{-1.3}$
9	20.7 ± 2.7	<18.1	<18.1	1.54 ± 0.19	<868.5	<216.9
10	23.6 ± 5.1	<9.3	<9.3	1.00 ± 0.24	<411.1	<105.3
11	20.1 ± 2.5	<16.2	<16.2	1.22 ± 0.18	<303.8	<103.7
12	30.8 ± 3.6	<1.8	<1.8	0.86 ± 0.13	<72.2	<19.2
13	22.8 ± 1.6	$11.0^{+3.3}_{-2.6}$	$11.0^{+3.3}_{-2.6}$	1.49 ± 0.13	$91.1^{+27.7}_{-21.2}$	$28.4^{+8.6}_{-6.6}$
14	26.0 ± 3.7	<6.5	<6.5	1.12 ± 0.17	<195.8	<57.2
15	22.3 ± 4.6	<8.6	<8.6	1.17 ± 0.27	<732.6	<151.3
16	25.8 ± 4.6	<5.1	<5.1	1.01 ± 0.20	<266.5	<64.8
17	17.6 ± 4.5	<21.9	<21.9	1.88 ± 0.57	<3516.3	<587.4
18	24.2 ± 4.5	<6.0	<6.0	1.12 ± 0.25	<477.4	<100.5
19	27.9 ± 2.3	$5.0^{+1.5}_{-1.2}$	$5.0^{+1.5}_{-1.2}$	1.28 ± 0.12	$48.8^{+14.8}_{-11.3}$	$14.4^{+4.4}_{-3.3}$
20	18.9 ± 5.3	<55.2	<55.2	1.90 ± 0.50	<8122.2	<1396.1

Note. The columns give the (1) source ID, (2) dust temperature, (3) total dust mass, (4) total gas mass, (5) index of emissivity (6) H_2 density, and (7) H_2 column density. The errors and upper limits are provided by 1σ and 3σ, respectively.

Table 4
Comparison between the Physical Properties of the SMC NEdeep and Wide-survey Objects

	This Study (NEdeep)	SMC Wide Survey
Cloud number	17	43
T_{dust} range	17.6–33.0 K	17–45 K
T_{dust} ave. ± std.	24.3 ± 4.4 K	28.7 ± 4.4 K
β range	0.9–1.9	1.2 (fixed)
β ave. ±std.	1.29 ± 0.29	…
M_{gas} range	(5.0–70) $\times 10^3 M_\odot$	(4.1–336) $\times 10^3 M_\odot$
M_{gas} median	11.0 $\times$ $10^3 M_\odot$	44.6 $\times$ $10^3 M_\odot$
R range	4–23 pc	6–40 pc
R median	7.1 pc	11.8 pc
H_2 density range	16–91 cm^{-3}	17–171 cm^{-3}
H_2 density ave. ±std. dev.	49 ± 29 cm^{-3}	68 ± 36 cm^{-3}
H_2 column density range	(13–28) $\times 10^{20}$ cm^{-2}	(10–44) $\times 10^{20}$ cm^{-2}
H_2 column density ave. ±std. dev.	(20 ± 6) $\times 10^{20}$ cm^{-2}	(29 ± 8) $\times 10^{20}$ cm^{-2}

Note. Upper-limit values of M_{gas}, H_2 density, and H_2 column density are excluded from the statistics.

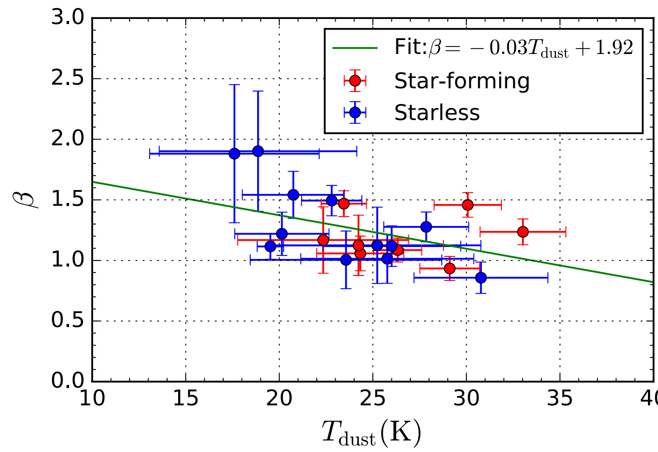

Figure 5. Relation between dust temperature and index of emissivity.

where the X_{CO} factor is 1×10^{21} cm^{-2} (K km s^{-1})$^{-1}$, which is reported by Muller et al. (2010) for the northeast region. This X_{CO} factor is also consistent with the estimate from the NANTEN CO and *Herschel* dust continuum (Mizuno et al. 2001; Roman-Duval et al. 2014).

A summary of the gas mass estimates using CO and dust is presented in Table 5 and Figure 6. The gas masses estimated using CO and dust are consistent with each other within errors of a factor of 2. Therefore, the gas masses estimated from the dust continuum can be used to estimate the total CO luminosity of dense clouds in the SMC. Thus, the assumption of a gas-to-dust ratio of 1000 and the X_{CO} factor of 1×10^{21} cm^{-2} (K km s^{-1})$^{-1}$, with uncertainties of a factor of 2, respectively, are reliable for estimating CO or continuum fluxes for future GMC studies. In contrast, these samples are biased in CO-detected objects, and the dust-selected clouds that have not been detected using CO lines are not included. Therefore, it is important to conduct further CO line observations on the CO-dark dust-selected cloud samples reported in this study and Takekoshi et al. (2017).

6.2. Internal Structure of the 1.1 mm Objects

We focus on the relationship among the dust, CO, and star formation in five CO-detected, dust-selected clouds in the SMC NE region by resolving the spatial structures. Figures 7 and 8 present the distributions of the dust properties (dust column density, dust temperature, and index of emissivity) and star formation tracers (*Spitzer* 24 μm, 8 μm, and Hα) of the 1.1 mm

Table 5
Comparison of Gas Masses Estimated from Dust and CO

Object ID	$M_{\rm gas,dust}$ ($10^3\ M_\odot$)	$M_{\rm gas,CO}$ ($10^3\ M_\odot$)	$M_{\rm gas,dust}/M_{\rm gas,CO}$	$L_{\rm CO}$ (10^2 K km s^{-1} pc^2)
NEdeep-4	$35.2^{+7.2}_{-6.0}$	44.2 ± 4.4	0.80	20.3 ± 2.3
NEdeep-5	$16.3^{+3.7}_{-3.0}$	9.1 ± 0.9	1.79	4.2 ± 0.4
NEdeep-7	$8.4^{+1.9}_{-1.5}$	10.7 ± 1.1	0.79	4.9 ± 0.5
NEdeep-9	<18.1	6.7 ± 0.7	…	3.1 ± 0.3
NEdeep-13	$11.0^{+3.3}_{-2.6}$	8.4 ± 0.8	1.31	3.9 ± 0.4

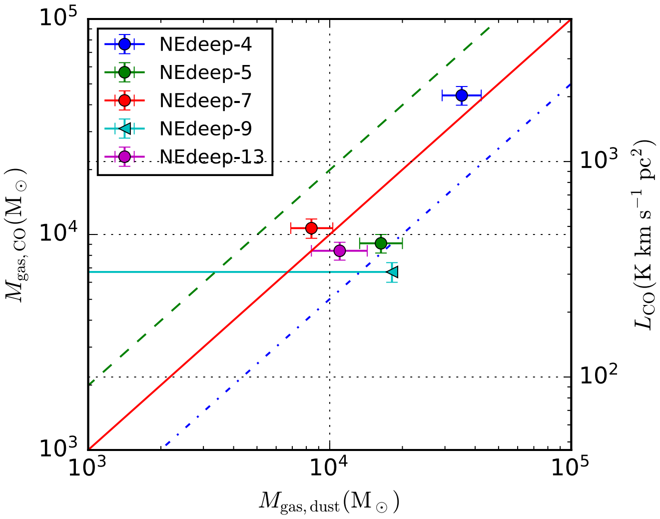

Figure 6. Comparison of gas mass estimated from dust and CO ($X_{\rm CO} = 1 \times 10^{21}$ cm^{-2} (K km s^{-1})$^{-1}$) of NEdeep objects. The range of CO luminosity is also shown on the right vertical axis. The lines show $M_{\rm gas,CO} = aM_{\rm gas,dust}$, with a = 1, 2, and 0.5 in solid (red), dashed (green), and dashed-dotted lines (blue), respectively.

objects that have already been detected in CO ($J = 1 - 0$) by NANTEN and Mopra (Mizuno et al. 2001; Muller et al. 2010).

6.2.1. Star Formation Activity

Here, we will examine the star formation activities of the CO-detected, dust-selected clouds. First, extended Hα emission is not observed in these dust clouds at a resolution of about 1 pc (3″–4″). By contrast, YSOs or bright 24 μm objects are present inside or near the dust-selected clouds. In particular, NEdeep-7 has a bright YSO at 24 μm on the east side of the object, and dust temperature is higher. Except for this object, we cannot find radio continuum emission at 8.64 and 4.8 GHz. In addition to the bright YSO in NEdeep-7, a YSO at the peak of NEdeep-5 may also affect the ISM because the dust temperature around this YSO is slightly higher than that in the other high column density regions. Although the existence of point-like Hα objects cannot disprove the existence of very compact H II regions, we can say that NEdeep-4, 9, and 13 are young evolution phases of GMCs that are not affected by the strong UV radiation from massive young stars. Therefore, these dust-selected clouds can be good candidates to investigate the initial conditions of massive star and cluster formation under low-metallicity environments.

In the CO-detected, dust-selected clouds in the SMC NE region, we were unable to find reliable starless objects. Takekoshi et al. (2017) also reported the lack of CO-detected and starless objects in the dust-selected cloud samples in the full SMC. A possible explanation is that the timescale of star formation (2–3 Myr) is shorter than that of CO molecule formation in the low-metallicity ISM, as pointed out in the numerical study of Glover & Clark (2012b).

6.2.2. Coincidence of Peak Positions Among Dust, CO, and Star Formation

In Figures 7 and 8, we notice that the CO-detected objects, except for NEdeep-7, show good agreement with the distributions between CO and the dust column density estimated from dust. This suggests that both CO and dust column density effectively trace dense molecular gas regions in GMCs. On the other hand, the positions of YSOs do not correspond to CO and dust column peaks. In particular, NEdeep-7 shows the distance between the YSO and the dust peak to be about 10 pc (∼30″), which is sufficiently larger than the pointing errors of <5″, <3″, and <1″ for the Mopra CO, cold dust (ASTE 1.1 mm and *Herschel*), and star formation tracers (*Spitzer*, Hα), respectively. This implies that the strong UV radiation from YSOs in NEdeep-7 affects the CO and cold dust distribution, but should be investigated by high-resolution studies in detail.

An interesting fact, particularly seen in NEdeep-4, is that the filamentary structure traced by 8 μm, which mainly traces emission from PAHs, shows good correlation with the CO emission. The spatial correlation between PAHs and CO emission has already been pointed out by previous low-metallicity ISM studies. Sandstrom et al. (2010) demonstrated that the PAH fraction spatially correlates with the CO intensity with a resolution of about 50 pc in the SMC. Recently, a low-metallicity (∼0.2 $Z_\odot$) dwarf galaxy, NGC 6822, was observed by a CO line using ALMA with a resolution of about 2 pc, reporting that the CO emission shows a better correlation with the 8 μm rather than the 24 μm and Hα (Schruba et al. 2017). These studies support the notion that PAH emissions effectively trace a photodissociated surface of dense molecular gas clouds observed by CO and dust continuum. Our result also indicates that PAH clumps or filamentary structures are good candidates for CO-emitting regions in low-metallicity ISM, although it also should be confirmed by high-resolution studies using ALMA.

We should also note that an extended dust component is found outside the PAH structures or CO emission. The most extended emission at 24 and 8 μm shows a good correspondence with the 1.1 mm objects. We can understand this extended dust emission as tracing the photodissociated surface of barely evolved gas clouds. The high dust column density implies the ability to form massive stars in the future but may not have yet formed compact, gravitationally bound filaments/clumps. In such regions, CO molecules would also not have formed yet, because of the long formation timescale of CO, as suggested by Glover & Clark (2012b).

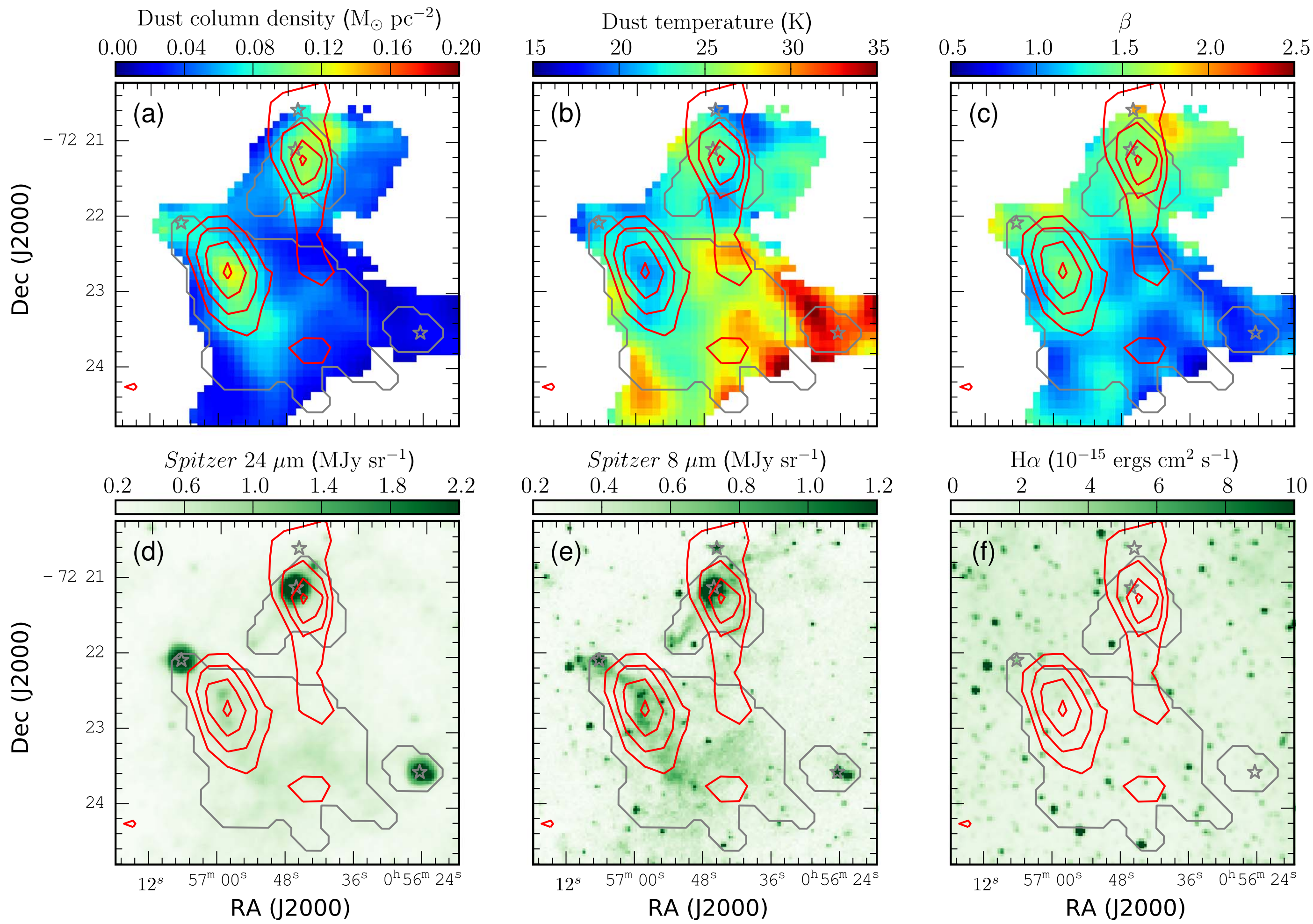

Figure 7. Spatial distribution of the (a) dust column density, (b) dust temperature, (c) index of emissivity, (d) *Spitzer* 24 μm, (e) *Spitzer* 8 μm, and (f) Hα in the NEdeep-4, 5, and 11 regions. The Mopra CO emission is represented by the red (150 km s^{-1} component) contours with a step of 0.5 K km s^{-1} starting from 2.5 K km s^{-1}. The gray contours represent the edges of the AzTEC 1.1 mm objects. The star symbols indicate the positions of YSOs (Bolatto et al. 2007; Sewiło et al. 2013).

7. Summary

The main results of this study are summarized below.

1. We obtained a 1.1 mm image using the AzTEC instrument on the ASTE telescope toward the SMC NE regions with an effective resolution of 40″ (∼12 pc). A median rms noise level of 1.3 mJy beam^{-1} was achieved for a field of 343 arcmin^2 (∼20′ × 20′).
2. We identified 20 objects in the observation region. Two NANTEN CO clouds that were not detected in a previous 1.1 mm survey were detected and resolved into multiple dust-selected clouds.
3. The dust mass and temperature were estimated by SED analysis using the MCMC method with the 1.1 mm, *Herschel*, and *Spitzer* data. Although the gas and dust masses of twelve 1.1 mm objects were estimated as upper limits, the other eight objects show the gas mass range of 5×10^3–$7 \times 10^4\,M_\odot$, assuming a gas-to-dust ratio of 1000. The ranges of the dust temperature and index of emissivity were 18–33 K and 0.9–1.9, respectively.
4. The 1.1 mm objects discovered by this study (NEdeep objects) show smaller dust masses and lower dust temperatures than the shallower 1.1 mm survey of Takekoshi et al. (2017). The fact that 40% of the 1.1 mm objects host YSOs, including relatively low-mass dust-selected clouds, suggests that the 1.1 mm objects trace dense gas clumps related to massive star formation.
5. The average of the index of emissivity is comparable to that in previous low-resolution studies in the SMC. The dust temperature and the index of emissivity shows a slightly negative correlation.
6. We investigated five dust-selected clouds that have already been detected by CO in detail. The total gas masses of the 1.1 mm objects estimated from the Mopra CO data are comparable to the gas masses estimated from the SED analysis of thermal dust emission. For the estimate of the total gas mass of molecular or dust-selected clouds, $X_{\rm CO} = 1 \times 10^{21}$ cm^{-2} (K km s^{-1})$^{-1}$ and a gas-to-dust ratio of 1000, with uncertainties of a factor of 2, are reliable in the SMC.
7. We compared the internal structure of dust-selected clouds estimated using an image-based SED fit with the Mopra CO and various star formation tracers. These objects exhibit no extended Hα emission, although they were associated with YSOs or 24 μm point sources, suggesting that these objects are young GMCs where star formation has just started; these are important targets for investigating the initial environment of massive star

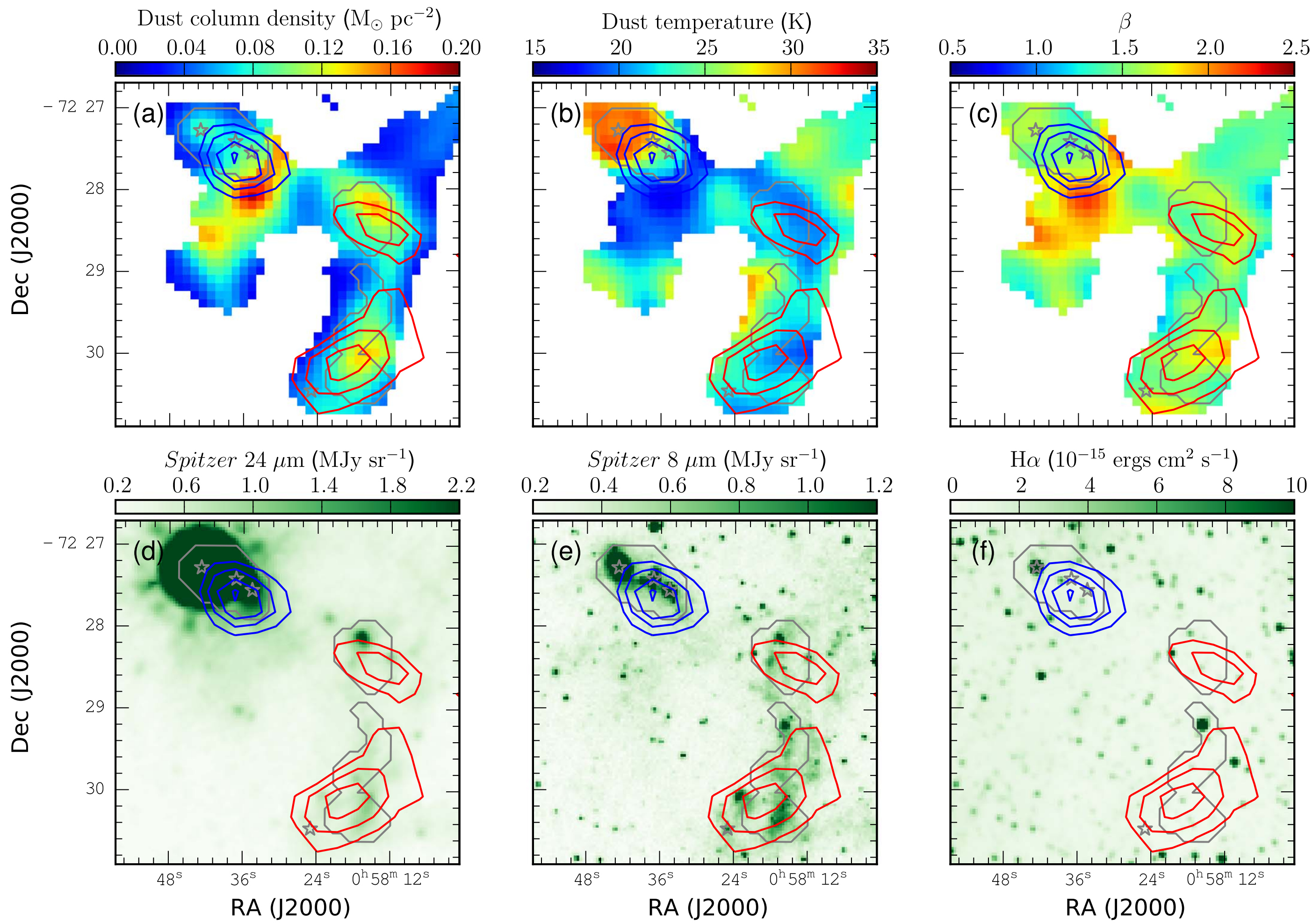

Figure 8. Spatial distribution of the (a) dust column density, (b) dust temperature, (c) index of emissivity, (d) *Spitzer* 24 μm, (e) *Spitzer* 8 μm, and (f) Hα in the NEdeep-7, 9, and 13 regions. The Mopra CO emission is represented by the red (150 km s^{-1} component) and blue (120 km s^{-1} component) contours with a step of 0.5 K km s^{-1} starting from 2.5 K km s^{-1}. The gray contours and star symbols are the same as the previous figure.

formation in low-metallicity environments. The dust column density shows good spatial correlation with CO emission except for NEdeep-7. The 8 μm filamentary structures and clumps show a similar spatial distribution to the CO emission and dust column density estimated using the image-based SED fits, implying that the filamentary structures or compact clumps traced by PAH emission are very good candidates of CO emitters. The extended emission at 24 and 8 μm, which do not show CO emission, exhibits a similar spatial distribution to the 1.1 mm objects, also suggesting that the cold gas component not yet affected by gravitational contraction in GMCs is also traced by the emission from very small grains and PAHs.

To obtain a more detailed understanding of the relation among cold dust, CO, and PAH emission, it is essential to conduct high-resolution CO and dust continuum observations toward the dust-selected clouds with ALMA, with a resolution comparable to the *Spitzer*/IRAC bands (∼1″).

The ASTE project was driven by NRO/NAOJ, in collaboration with the University of Chile and Japanese institutes including the University of Tokyo, Nagoya University, Osaka Prefecture University, Ibaraki University, Hokkaido University, and Joetsu University of Education. Observations with ASTE were carried out remotely from Japan using NTT's GEMnet2 and its partner R&E networks, which are based on the AccessNova collaboration among the University of Chile, NTT Laboratories, and NAOJ. This work is based on data products made with the *Spitzer Space Telescope* (JPL/Caltech under a contract with NASA). Data analysis was, in part, carried out on the open-use data analysis computer system at the Astronomy Data Center, ADC, of the National Astronomical Observatory of Japan. This research made use of the SIMBAD database, operated at CDS, Strasbourg, France. This research made use of Astropy, a community-developed core Python package for Astronomy (Astropy Collaboration et al. 2013). This study was supported by the MEXT Grant-in-Aid for Specially Promoted Research JP20001003 and the JSPS Grant-in-Aid for Scientific Research (S) JP17H06130. M.R. acknowledges support from CONICYT (CHILE) through FONDECYT grant N^{o}1140839.

Facilities: ASTE, *Spitzer* (MIPS, IRAC), *Herschel* (SPIRE, PACS), MOPRA, ATCA, Parkes.

Software: IDL, Astropy (Astropy Collaboration et al. 2013), PyMC3 (Salvatier et al. 2016), NumPy (Walt et al. 2011), SciPy (Jones et al. 2001), Matplotlib (Hunter 2007).

ORCID iDs

Tatsuya Takekoshi https://orcid.org/0000-0002-4124-797X
Tetsuhiro Minamidani https://orcid.org/0000-0001-9778-6692
Kotaro Kohno https://orcid.org/0000-0002-4052-2394
Tomoka Tosaki https://orcid.org/0000-0001-9016-2641
Caroline Bot https://orcid.org/0000-0001-6118-2985
Itziar Aretxaga https://orcid.org/0000-0002-6590-3994
Min S. Yun https://orcid.org/0000-0001-7095-7543

References

Aguirre, J. E., Bezaire, J. J., Cheng, E. S., et al. 2003, ApJ, 596, 273
Astropy Collaboration, Robitaille, T. P., Tollerud, E. J., et al. 2013, A&A, 558, A33
Bolatto, A. D., Simon, J. D., Stanimirović, S., et al. 2007, ApJ, 655, 212
Bot, C., Boulanger, F., Rubio, M., & Rantakyro, F. 2007, A&A, 471, 103
Bot, C., Rubio, M., Boulanger, F., et al. 2010a, A&A, 524, A52
Bot, C., Ysard, N., Paradis, D., et al. 2010b, A&A, 523, A20
Dickel, J. R., Gruendl, R. A., McIntyre, V. J., & Amy, S. W. 2010, AJ, 140, 1511
Downes, T. P., Welch, D., Scott, K. S., et al. 2012, MNRAS, 423, 529
Draine, B. T., Aniano, G., Krause, O., et al. 2014, ApJ, 780, 172
Draine, B. T., & Lee, H. M. 1984, ApJ, 285, 89
Draine, B. T., & Li, A. 2007, ApJ, 657, 810
Ezawa, H., Kawabe, R., Kohno, K., & Yamamoto, S. 2004, Proc. SPIE, 5489, 763
Ezawa, H., Kohno, K., Kawabe, R., et al. 2008, Proc. SPIE, 7012, 701208
Fukui, Y., & Kawamura, A. 2010, ARA&A, 48, 547
Glover, S. C. O., & Clark, P. C. 2012a, MNRAS, 421, 9
Glover, S. C. O., & Clark, P. C. 2012b, MNRAS, 426, 377
Gordon, K. D., Meixner, M., Meade, M. R., et al. 2011, AJ, 142, 102
Gordon, K. D., Roman-Duval, J., Bot, C., et al. 2014, ApJ, 797, 85
Gordon, K. D., Roman-Duval, J., Bot, C., et al. 2017, ApJ, 837, 98
Hilditch, R. W., Howarth, I. D., & Harries, T. J. 2005, MNRAS, 357, 304
Hony, S., Gouliermis, D. A., Galliano, F., et al. 2015, MNRAS, 448, 1847
Hunter, J. D. 2007, CSE, 9, 90
Israel, F. P., Johansson, L. E. B., Lequeux, J., et al. 1993, A&A, 276, 25
Israel, F. P., Johansson, L. E. B., Rubio, M., et al. 2003, A&A, 406, 817
Israel, F. P., Wall, W. F., Raban, D., et al. 2010, A&A, 519, A67
Jones, E., Oliphant, T., Peterson, P., et al. 2001, SciPy: Open Source Scientific Tools for Python, http://www.scipy.org/
Juvela, M., Montillaud, J., Ysard, N., & Lunttila, T. 2013, A&A, 556, A63
Juvela, M., & Ysard, N. 2012, A&A, 539, A71
Kelly, B. C., Shetty, R., Stutz, A. M., et al. 2012, ApJ, 752, 55
Komugi, S., Tosaki, T., Kohno, K., et al. 2011, PASJ, 63, 1139
Kurt, C. M., Dufour, R. J., Garnett, D. R., et al. 1999, ApJ, 518, 246
Larsen, S. S., Clausen, J. V., & Storm, J. 2000, A&A, 364, 455
Le Coarer, E., Rosado, M., Georgelin, Y., Viale, A., & Goldes, G. 1993, A&A, 280, 365
Lequeux, J., Le Bourlot, J., Pineau des Forets, G., et al. 1994, A&A, 292, 371
Leroy, A., Bolatto, A., Stanimirovic, S., et al. 2007, ApJ, 658, 1027
Liu, G., Calzetti, D., Yun, M. S., et al. 2010, AJ, 139, 1190
Malinen, J., Juvela, M., Collins, D. C., Lunttila, T., & Padoan, P. 2011, A&A, 530, A101
Meixner, M., Panuzzo, P., Roman-Duval, J., et al. 2013, AJ, 146, 62
Mizuno, N., Rubio, M., Mizuno, A., et al. 2001, PASJ, 53, L45
Muller, E., Ott, J., Hughes, A., et al. 2010, ApJ, 712, 1248
Muller, E., Staveley-Smith, L., & Zealey, W. J. 2003, MNRAS, 338, 609
Muller, E., Wong, T., Hughes, A., et al. 2013, in IAU Symp. 292, Molecular Gas, Dust, and Star Formation in Galaxies, ed. T. Wong & J. Ott (Cambridge: Cambridge Univ. Press), 110
Planck Collaboration, Ade, P. A. R., Aghanim, N., et al. 2011, A&A, 536, A17
Roman-Duval, J., Gordon, K. D., Meixner, M., et al. 2014, ApJ, 797, 86
Rubio, M., Boulanger, F., Rantakyro, F., & Contursi, A. 2004, A&A, 425, L1
Rubio, M., Contursi, A., Lequeux, J., et al. 2000, A&A, 359, 1139
Rubio, M., Garay, G., Montani, J., & Thaddeus, P. 1991, ApJ, 368, 173
Rubio, M., Lequeux, J., & Boulanger, F. 1993a, A&A, 271, 9
Rubio, M., Lequeux, J., Boulanger, F., et al. 1993b, A&A, 271, 1
Rubio, M., Lequeux, J., Boulanger, F., et al. 1996, A&AS, 118, 263
Salvatier, J., Wiecki, T. V., & Fonnesbeck, C. 2016, PeerJ Comput. Sci., 2, e55
Sandstrom, K. M., Bolatto, A. D., Draine, B. T., Bot, C., & Stanimirović, S. 2010, ApJ, 715, 701
Schruba, A., Leroy, A. K., Kruijssen, J. M. D., et al. 2017, ApJ, 835, 278
Scott, K. S., Austermann, J. E., Perera, T. A., et al. 2008, MNRAS, 385, 2225
Sewiło, M., Carlson, L. R., Seale, J. P., et al. 2013, ApJ, 778, 15
Shetty, R., Kauffmann, J., Schnee, S., & Goodman, A. A. 2009a, ApJ, 696, 676
Shetty, R., Kauffmann, J., Schnee, S., Goodman, A. A., & Ercolano, B. 2009b, ApJ, 696, 2234
Shimajiri, Y., Kawabe, R., Takakuwa, S., et al. 2011, PASJ, 63, 105
Smith, C., Leiton, R., & Pizarro, S. 2000, in ASP Conf. Ser. 221, Stars, Gas and Dust in Galaxies: Exploring the Links, ed. D. Alloin, K. Olsen, & G. Galaz (San Francisco, CA: ASP), 83
Takekoshi, T., Minamidani, T., Komugi, S., et al. 2017, ApJ, 835, 55
Vangioni-Flam, E., Lequeux, J., Maucherat-Joubert, M., & Rocca-Volmerange, B. 1980, A&A, 90, 73
Walt, S. v. d., Colbert, S. C., & Varoquaux, G. 2011, CSE, 13, 22
Wilson, G. W., Austermann, J. E., Perera, T. A., et al. 2008a, MNRAS, 386, 807
Wilson, G. W., Hughes, D. H., Aretxaga, I., et al. 2008b, MNRAS, 390, 1061